

---

This is an electronic reprint of the original article.  
This reprint may differ from the original in pagination and typographic detail.

Verkama, Emma; Järvinen, Ellen; Albersberger, Sylvia; Meinander, Kristoffer; Jiang, Hua; Tiitta, Marja; Karinen, Reetta; Puurunen, Riikka L.

## Hydrodeoxygenation and hydrodenitrogenation of n-hexadecanamide to n-paraffins: Bimetallic catalysts supported on ceria-zirconia

*Published in:*  
Applied Catalysis A: General

*DOI:*  
[10.1016/j.apcata.2024.119602](https://doi.org/10.1016/j.apcata.2024.119602)

Published: 25/04/2024

*Document Version*  
Publisher's PDF, also known as Version of record

*Published under the following license:*  
CC BY

*Please cite the original version:*  
Verkama, E., Järvinen, E., Albersberger, S., Meinander, K., Jiang, H., Tiitta, M., Karinen, R., & Puurunen, R. L. (2024). Hydrodeoxygenation and hydrodenitrogenation of n-hexadecanamide to n-paraffins: Bimetallic catalysts supported on ceria-zirconia. *Applied Catalysis A: General*, 676, Article 119602.  
<https://doi.org/10.1016/j.apcata.2024.119602>

---

This material is protected by copyright and other intellectual property rights, and duplication or sale of all or part of any of the repository collections is not permitted, except that material may be duplicated by you for your research use or educational purposes in electronic or print form. You must obtain permission for any other use. Electronic or print copies may not be offered, whether for sale or otherwise to anyone who is not an authorised user.



# Hydrodeoxygenation and hydrodenitrogenation of *n*-hexadecanamide to *n*-paraffins: Bimetallic catalysts supported on ceria-zirconia

Emma Verkama<sup>a,\*</sup>, Ellen Järvinen<sup>a</sup>, Sylvia Albersberger<sup>b</sup>, Kristoffer Meinander<sup>c</sup>, Hua Jiang<sup>d</sup>, Marja Tiitta<sup>b,1</sup>, Reetta Karinen<sup>a</sup>, Riikka L. Puurunen<sup>a</sup>

<sup>a</sup> Department of Chemical and Metallurgical Engineering, School of Chemical Engineering, Aalto University, P.O. Box 16100, 00076 Aalto, Finland

<sup>b</sup> Neste Corporation, P.O. Box 310, 06101 Porvoo, Finland

<sup>c</sup> Department of Bioproducts and Biosystems, School of Chemical Engineering, Aalto University, P.O. Box 16300, 00076 Aalto, Finland

<sup>d</sup> Department of Applied Physics, School of Science, Aalto University, P.O. Box 13500, 00076 Aalto, Finland

## ARTICLE INFO

### Keywords:

Amide  
Hydrodenitrogenation  
Hydrodeoxygenation  
Bimetallic catalyst  
CeO<sub>2</sub>-ZrO<sub>2</sub>

## ABSTRACT

The development of catalysts for simultaneous hydrodeoxygenation (HDO) and hydrodenitrogenation (HDN) is relevant for the production of renewable fuels. In this work, the activity of CeO<sub>2</sub>-ZrO<sub>2</sub> supported Pt, Co, PtCo, Cu, PtCu, Ni, PtNi, Ru and RuNi catalysts was studied in the hydrotreatment of *n*-hexadecanamide at 300 °C and 80 bar H<sub>2</sub>. The bimetallic catalysts differed from the corresponding monometallic catalysts in terms of activity and selectivity. PtCu was less active than the monometallic Pt catalyst, as the addition of Cu suppressed the activity for hydrogenolysis reactions. Pt and PtCo showed a similar activity but a remarkably different selectivity, with Pt favoring *n*-hexadecane and PtCo favoring *n*-pentadecane. The RuNi and PtNi catalysts exhibited a higher nitrogen removal and an improved selectivity for *n*-pentadecane compared to the corresponding monometallic catalysts, emphasizing the potential of catalysts containing Ni and a noble metal. Furthermore, the formation of C32 compounds was limited on RuNi.

## 1. Introduction

Nitrogen-containing compounds, such as fatty amides, are present in feedstocks that can be upgraded to renewable fuels via hydrotreating [1, 2]. These feedstocks include, e.g., animal fats and algal biocrudes [1,2]. Published research on simultaneous hydrodeoxygenation (HDO) and hydrodenitrogenation (HDN) of molecules which include both oxygen and nitrogen is, nevertheless, limited [3–8]. The hydrotreatment of *n*-hexadecanamide (C16 amide) on Pt catalysts supported on different metal oxides, and on various metals supported on ZrO<sub>2</sub>, was studied in recent articles by Verkama et al. [7,8] The catalyst support had an impact on the pathway selectivity for the initial conversion of the C16 amide to oxygen-containing and nitrogen-containing intermediate products, and on the activity for the HDO of the oxygen containing intermediate products. The Pt/CeO<sub>2</sub>-ZrO<sub>2</sub> catalyst exhibited a high activity, particularly in HDO reactions, which was attributed to the weak Lewis acid sites on the CeO<sub>2</sub>-ZrO<sub>2</sub> support [7]. The active metal, in turn, influenced the preference for condensation reactions and the C–C, C–O and C–N bond cleavage routes in the formation of paraffins [8]. Pt and

Ru, which favored the formation of the C16 and C15 *n*-paraffins, respectively, were identified as promising active metals for the hydrotreatment of the C16 amide [8]. The overall activity was, however, limited by the activity for the HDN of the nitrogen-containing intermediate products, and in the case of Pt, the formation of C32 condensation products [3,7,8]. The activity of supported Pt and Ru catalysts has additionally been widely demonstrated in, e.g., the HDO of vegetable oils and fatty acids [9–12].

Bimetallic catalysts can exhibit an enhanced activity, selectivity and stability compared to corresponding monometallic systems [13–25]. The formation of heteroatom bonds alters the electronic environment and geometry of bimetallic surfaces compared to the monometallic counterparts, which influences the adsorption strength and the adsorption mode of reactants and intermediates [13–15]. The catalytic properties of bimetallic particles can also be related to synergistic effects, where both metals participate in the bonding with the reaction intermediates or transition states, or to bifunctional effects, where the metals are responsible for different functions in the reaction mechanism [14,15]. The structure of supported bimetallic particles can be complex,

\* Corresponding author.

E-mail address: [emma.verkama@aalto.fi](mailto:emma.verkama@aalto.fi) (E. Verkama).

<sup>1</sup> Present address: Hamari, Finland

<https://doi.org/10.1016/j.apcata.2024.119602>

Received 29 November 2023; Received in revised form 31 January 2024; Accepted 3 February 2024

Available online 7 February 2024

0926-860X/© 2024 The Authors. Published by Elsevier B.V. This is an open access article under the CC BY license (<http://creativecommons.org/licenses/by/4.0/>).

which makes the formulation of structure–activity relationships challenging [15].

Promising results have been reported for the activity of bimetallic catalysts, such as PtNi, PtCo and RuNi, in HDO reactions [17–23,26] and in the hydrogenation of nitriles and amides to amines [24,25,27,28]. For example, Do et al. [18] studied the HDO of *meta*-cresol on  $\gamma$ -Al<sub>2</sub>O<sub>3</sub> supported Pt, Co, PtCo, Ni and PtNi catalysts. The bimetallic catalysts showed a higher HDO activity and a different selectivity compared to the corresponding monometallic catalysts, which resulted from an enhanced hydrogenation activity and the formation of active sites for the dehydration of alcohols [18]. Particularly, the reaction rate of PtCo substantially exceeded the sum of the reaction rates of the monometallic Pt and Co catalysts [18]. Li et al. [20] reported that a bimetallic RuNi/SiO<sub>2</sub>-ZrO<sub>2</sub> catalyst showed a high activity in the HDO of guaiacol, which could be related to electron transfer from Ru to Ni promoting the adsorption and activation of hydrogen and the reactant. Electronic interactions between the active metals in bimetallic PdPt and PtNi catalysts have also been suggested to improve the resistance to deactivation via sulfur poisoning and coking, compared to corresponding monometallic catalysts [13,23,29]. Considering the performance of monometallic Pt and Ru catalysts in the hydrotreatment of the C16 amide [7, 8], and the activity of bimetallic Pt and Ru based catalysts in HDO reactions [17–23,26], it can be hypothesized that bimetallic Pt and Ru based catalysts could exhibit a high activity and paraffin selectivity in the hydrotreatment of fatty amides.

To our knowledge, the activity of reduced bimetallic catalysts has not been previously studied for the HDO and HDN of fatty amides to *n*-paraffins. Therefore, the purpose of this work was to assess bimetallic effects in CeO<sub>2</sub>-ZrO<sub>2</sub> supported PtCu, PtCo, PtNi and RuNi catalysts in the hydrotreatment of the C16 amide. The CeO<sub>2</sub>-ZrO<sub>2</sub> support was chosen based on the results of a previous work by Verkama et al. [7] Herein, we demonstrate the activity and paraffin selectivity of bimetallic catalysts supported on CeO<sub>2</sub>-ZrO<sub>2</sub> in the hydrotreatment of primary amides to *n*-paraffins. This work emphasizes the potential of bimetallic catalysts for the simultaneous HDO and HDN of renewable feedstocks to fuels.

## 2. Experimental

### 2.1. Materials

Cerium-zirconium oxide (CeO<sub>2</sub>-ZrO<sub>2</sub>) with 17 wt% CeO<sub>2</sub> (MEL Chemicals, XZO 1289) was used as the catalyst support. The metal precursors were platinum(IV) nitrate solution (15 wt% Pt) and ruthenium(III) nitrosyl nitrate (31.78 wt% Ru) from Alfa Aesar, nickel(II) nitrate hexahydrate (99.999%) and copper(II) nitrate trihydrate (98.0–103%) from Aldrich, and cobalt(II) nitrate hexahydrate (>99%) from Merck.

The following chemicals were used without further purification for the reactor experiments and calibrations: *n*-hexadecanamide (>95%, Tokyo Chemical Industry), 1-hexadecylamine (>95%, Tokyo Chemical Industry), *n*-pentadecane (>99%, Aldrich), *n*-hexadecane (>99%, Sigma Aldrich), *n*-hexadecanal (>97%, Tokyo Chemical Industry), 1-hexadecanol (96%, Acros Organics), palmitic acid (>98%, Riedel de Haën), *n*-pentadecanonitrile (>95%, Tokyo Chemical Industry), *n*-heptadecanonitrile (>95%, Tokyo Chemical Industry), decalin (decahydronaphthalene, *cis* + *trans*, 98%, Thermo Scientific), *n*-dodecane (>99%, Merck) and 2-propanol (>99%, Riedel de Haën). The pyridine that was used for acid site characterization was obtained from Sigma Aldrich (anhydrous, 99.8%).

The helium (99.999%) and synthetic air (99.999%) that were used in the pyridine FTIR measurements were from Linde. The hydrogen, nitrogen, helium, synthetic air, argon and oxygen that were used for the reactor experiments, product analysis and for the other catalyst characterization methods were of purity 99.999% and purchased from Woikoski. The 2 vol% H<sub>2</sub>/Ar (99.999%/99.999%), 5.2 vol% CO<sub>2</sub>/He

(99.999%/99.999%) and the 10 vol% CO/He (99.999%/99.999%) gas mixtures were likewise acquired from Woikoski.

### 2.2. Catalyst preparation

The CeO<sub>2</sub>-ZrO<sub>2</sub> support was sieved to a particle size of 0.25–0.42 mm and calcined at 450 °C in ambient air in a static muffle furnace for 10 h prior to impregnation. The catalysts were prepared by incipient wetness impregnation, targeting metal loadings of 0.5 wt% for Pt and Ru, and 1.5 wt% for Cu, Co and Ni. The metals were co-impregnated in case of the bimetallic catalysts. The metal precursor solutions were prepared with Type 1 ultrapure water, with a volume that matched the pore volume of the support. The impregnation solution was introduced dropwise to the support, stirring vigorously between the additions. The catalysts were aged at room temperature overnight and dried in an oven for 5 h at 120 °C. The catalysts were calcined in a flow through calcination oven under a 100 ml/min flow of synthetic air at 450 °C for 2 h, using a 1 °C/min heating rate.

### 2.3. Catalyst characterization

The catalysts were characterized with N<sub>2</sub> physisorption, CO pulse titration measurements, scanning transmission electron microscopy (STEM), X-ray fluorescence (XRF), X-ray diffraction (XRD), hydrogen temperature-programmed reduction (H<sub>2</sub>-TPR), Fourier transform infrared spectroscopy (FTIR), temperature programmed desorption of CO<sub>2</sub> (CO<sub>2</sub>-TPD) and X-ray photoelectron spectroscopy (XPS), as described in detail in previous works by Verkama et al. [7,8] The method descriptions are repeated below for clarity.

Isothermal N<sub>2</sub> physisorption measurements were performed in a Surfer equipment from Thermo Scientific. The analysis was conducted at –196 °C for 100 mg samples of the calcined catalysts, using liquid nitrogen as a coolant. Prior to the measurements, the samples were degassed in vacuum at 350 °C for 180 min, using a 5 °C/min heating rate, with the aim of removing moisture and other adsorbed compounds. Dead volume calibrations were carried out with He for every measurement. The specific surface area (*S*<sub>BET</sub>, m<sup>2</sup>/g) of the samples was calculated from the adsorption isotherms with the Brunauer–Emmett–Teller method [30], while the Barrett–Joyner–Halenda method [31] was used to calculate the pore size distribution, mean pore diameter (*d*<sub>pore, mean</sub>, nm) and pore volume (*V*<sub>pore</sub>, cm<sup>3</sup>/g) from the desorption branch.

CO pulse titrations were carried out for 100 mg catalyst samples. The measurements were done in an AMI-200R flow through equipment from Altamira Instruments, which was connected to a Pfeiffer OmniStar GSD320 mass spectrometer (MS). Prior to the titration, the samples were dried at 200 °C in He for 120 min, reduced at 350 °C in 2 vol% H<sub>2</sub>/Ar for 60 min, cooled down to 30 °C and held in He for 60 min. Next, 30 pulses of 2 vol% or 5 vol% CO/He (0.505 ml, 30 °C) were introduced to the samples with 5-min intervals, while monitoring the composition of the gas flow with the MS (*m/z* 28 for CO, 44 for CO<sub>2</sub>, and 18 for H<sub>2</sub>O). The carrier gas flow was maintained at 50 ml/min (STP) throughout the measurement.

High angle annular dark-field (HAADF) STEM images were taken of the calcined catalysts, using a JEOL JEM-2200FS aberration corrected high resolution electron microscope operating at 200 kV acceleration voltage. The microscope is coupled with an X-ray energy-dispersive spectrometer (EDS) for elemental mapping analysis. For the microscopy measurements, the samples were drop-casted with acetone on copper grids coated with ultrathin carbon film.

The active metal loading was measured semi-quantitatively with XRF, using a wavelength dispersive PANalytical Axios mAx equipment. The measurements were conducted in He for approximately 250 mg catalyst samples of the ground, calcined catalysts. For the measurements, the loose powder samples were placed in Chemplex 1330-SE sample cups covered with a 3.6 μm mylar film. The data of the powder XRF measurements is semi-quantitative due to matrix effects [32].

The results can be used to compare the content of a given element between samples, but not necessarily the content of different elements.

XRD was used to study the crystallographic phases of ground samples of the calcined catalysts. A PANalytical X'Pert PRO MPD Alpha-1 X-ray diffractometer with Cu K $\alpha$ 1 radiation (45 kV, 40 mA) was used and the measurements were performed for a 2 $\theta$  scanning range from 5° to 100°, using a step size of 0.026°. The HighScore software was used to identify the crystallographic phases of the samples (ICDD PDF-4 + 2023 database).

The reducibility of the catalysts was qualitatively studied with H<sub>2</sub>-TPR. The measurements were done in the AMI-200R equipment for 100 mg samples of the calcined catalysts. The samples were first heated from room temperature to 200 °C in He flow with a heating rate of 10 °C/min and held for 120 min. Afterwards, the samples were cooled down to 30 °C in 50 ml/min He and flushed in Ar for 30 min. A flow of 2 vol% H<sub>2</sub>/Ar was then introduced to the samples, and the temperature was elevated from 30 °C to 600 °C with a heating rate of 5 °C/min. The total flowrate was maintained constant throughout the measurement (50 ml/min STP). To monitor the H<sub>2</sub> consumption,  $m/z$  2 was followed with the Pfeiffer OmniStar GSD320 MS. Additionally,  $m/z$  4 (He),  $m/z$  18 (H<sub>2</sub>O),  $m/z$  28 (N<sub>2</sub>/CO),  $m/z$  32 (O<sub>2</sub>) and  $m/z$  40 (Ar) were followed.

Transmission FTIR measurements using pyridine as the probe molecule were carried out to quantify the acidity of the catalysts. The measurements were performed with a Thermo Scientific Nicolet iS10 spectrometer, which was equipped with an in-situ transmission FTIR cell by Harrick Scientific Products Inc (customized from the HTC-3 model), a liquid-N<sub>2</sub> cooled Mercury-Cadmium-Telluride (MCT) detector and a HeNe laser. The spectra range was 4000–650 cm<sup>-1</sup>, and the spectral resolution was 0.24 cm<sup>-1</sup>. Approximately 25 mg samples of the calcined catalysts were ground and pressed into self-supported pellets with a diameter of 1.1 cm. The samples were heated to 90 °C in vacuum with a heating rate of 5 °C/min, and maintained at 90 °C for 30 min. Then, the temperature was elevated to 450 °C with a rate of 20 °C/min and kept at 450 °C for 60 min. Next, the temperature was lowered to 170 °C, where it was held for 10 min, after of which the spectra of the clean samples were collected. The samples were then saturated with pyridine for 10 min, using an atmospheric saturator, which was followed by evacuation and a 15 min hold. The spectra that were used to quantify the acidity were then collected. The background and the spectra of the clean samples were subtracted from the spectra of the pyridine-saturated samples, and a stepwise linear baseline correction was carried out and the peak areas were integrated using the Omnic 9.11 software. The data was deconvoluted using OriginPro. Table S1 of the Supplementary Materials displays the deconvolution details. The concentration of Lewis and Brønsted acid sites were estimated from the corresponding peak areas and the sample weight, as outlined by Emeis [33].

The CO<sub>2</sub>-TPD measurements were conducted for the catalysts to quantify their overall basicity. The measurements were done with the AMI-200R equipment. The sample amount was 100 mg. The samples were dried in He for 2 h at 180 °C, using a heating rate of 10 °C/min. Then, the samples were reduced for 2 h at 350 °C in 2 vol% H<sub>2</sub>/Ar. After the reduction, the samples were cooled down in He to 50 °C and further held for 30 min. Next, a 0.52 vol% CO<sub>2</sub>/He flow was directed to the samples at 50 °C and maintained for 60 min, after of which the samples were flushed in He for 60 min. Then, the samples were heated to 800 °C in He with a heating rate of 10 °C/min, which was followed by an isothermal hold at 800 °C for 30 min before cooling down. A 50 ml/min (STP) gas flow was maintained throughout the entire measurement. A one-step calibration was carried out for the  $m/z$  44 signal of the Pfeiffer OmniStar GSD320 MS to quantify the amount of desorbed CO<sub>2</sub>. The data was deconvoluted using OriginPro. Table S2 of the Supplementary Materials shows the deconvolution details.

The chemical state of the catalyst surface was studied by XPS. Before the measurements, the samples were reduced ex-situ in 2 vol% H<sub>2</sub> at 350 °C for 60 min. The samples were transferred to the equipment exposed to atmosphere. The measurements were performed with a

Kratos AXIS Ultra DLD X-ray photoelectron spectrometer using a monochromated AlK $\alpha$  X-ray source (1486.7 eV) run at 100 W, as described previously [7]. For the survey spectra, a pass energy of 80 eV and a step size of 1.0 eV were used, while a pass energy of 20 eV and a step size of 0.1 eV were used for the high-resolution spectra. Photoelectrons were collected at a 90° take-off angle under ultra-high vacuum conditions, with a base pressure below 1 × 10<sup>-9</sup> Torr. The diameter of the beam spot from the X-ray was 1 mm, and the area of analysis was 300 μm × 700 μm. Both survey and high-resolution spectra were collected from three different spots the samples. The spectra were charge-corrected relative to the position of C–C bonding of carbon at 284.8 eV.

The C 1s spectra were fitted with four Gaussian components according to standard tabulated chemical shifts, with peak positions at 284.8 eV (C–C), 286.5 eV (C–O), 287.8 eV (C=O), and 288.9 eV (O–C=O). The Zr 3d spectra were fitted with two doublets, with the 3d<sub>5/2</sub> peaks located at 181.8 eV and 183.0 eV. The lower binding energy component corresponds to ZrO<sub>2</sub>, while the higher binding energy component most likely is related to a mixed oxide state with a slightly lower electron density surrounding the Zr ions. For the Ce 3d spectra, a fitting scheme similar to that of Béche et al. [34] was used to differentiate between Ce(III) and Ce(IV) oxides. The O 1s spectra was deconvoluted using three Gaussian components, related to lattice oxygen, surface hydroxyls (+1.5 eV) and to oxygen bound to organic contaminants (+2.75 eV).

The Pt 4f spectra were fitted using five doublets, for metallic Pt(0), Pt(I), Pt(II), Pt(IV), and for a mixed state located between Pt(I) and Pt(II), with binding energies for the Pt 4f<sub>7/2</sub> component located at approximately 71.0 eV, 72.2 eV, 73.5 eV, 74.5 eV, and 72.7 eV, respectively. The Ru 3d components were deconvoluted together with the C 1s components. Two doublets with the 3d<sub>5/2</sub> energies at 279.8 eV and 280.9 eV were used for Ru(0) and Ru(IV), respectively. The Ni 2p spectra were deconvoluted using three components, with the 2p<sub>3/2</sub> peaks at energies of 852.8 eV, 853.9 eV, and 856.6 eV, attributed to Ni(0), Ni(II) and Ni(III), respectively. Each main peak was coupled to a corresponding satellite peak, with a fixed area ratio and energy difference compared to the main peak. The Co 2p spectra were fitted with multiple peaks as outlined by Biesinger et al. [35]. The sharp peak at approximately 932.1 eV of the Cu 2p<sub>3/2</sub> spectra was attributed to Cu(I), but due to the similarity in binding energy, the presence of metallic Cu(0) cannot be entirely excluded. A broadening of the peak and a satellite at around 942 eV, associated with Cu(II), was also present.

#### 2.4. Catalytic activity tests and product analysis

The catalytic activity tests were carried out in a 100 ml Hastelloy high-pressure batch reactor by Parr Instrument Company, using *n*-hexadecanamide (100 ppm N) as a model compound and decalin as a solvent (30 ml). Before the activity tests, the catalysts (20 mg) were first dried at 180 °C in 10 bar N<sub>2</sub> for 60 min, and reduced at 350 °C in 20 bar H<sub>2</sub> for 60 min. The reactions were done at 300 °C and 80 bar H<sub>2</sub>, as described in a previous work by Verkama et al. [7] Reaction times between 15 and 300 min were studied, and the 60 min experiments were used as a basis for the activity comparison. For the most active catalysts, the reactions were stopped after the total paraffin yield exceeded 80% (90 min for RuNi and 180 min for PtNi). The experiments with different reaction times were visualized with respect to the batch residence time ( $\tau$ ,  $g_{\text{cat}}h/g_{\text{amide}}$ ), as defined in Eq. (1), in order to account for variations in the catalyst amount and model compound concentration.

$$\tau = \frac{m_{\text{cat}}t}{m_A} \quad (1)$$

Here,  $m_{\text{cat}}$  is the mass of catalyst (g),  $t$  is the reaction time (h) and  $m_A$  is the mass of reactant at the start of the reaction (g).

The reaction products were quantified using gas chromatography with flame ionization detection (GC-FID) and the total nitrogen content was measured with a total nitrogen content analyzer [3,7]. The reactant

conversion ( $X_A$ , %), product yields ( $Y_P$ , %) and oxygen removal ( $O$ -removal, %) were derived from the GC-FID analysis results, while the nitrogen removal ( $N$ -removal, %) was calculated from the total nitrogen content analysis, as described previously [3,7].

### 3. Results and discussion

#### 3.1. Catalyst characterization

The target metal loading and semi-quantitative metal loading from XRF measurements, the specific surface area, pore volume and mean pore diameter from  $N_2$  physisorption measurements, and the CO adsorption capacity from CO pulse titration measurements are presented in Table 1 for the catalysts. Table 1 additionally contains the desorbed amount of  $CO_2$  from  $CO_2$ -TPD measurements, which is used as a measure of the total basicity, and the amount of pyridine adsorbed on Brønsted acid sites (BAS) and Lewis acid sites (LAS) from the pyridine FTIR measurements.

The semi-quantitative elemental analysis indicated that the metal content of the bimetallic catalysts was comparable to the sum of the metal contents of the corresponding monometallic catalysts (Table 1). The specific surface area (78–88  $m^2/g$ ), pore volume (0.17–0.21  $cm^3/g$ ) and mean pore size (7.8–8.5 nm) of the catalysts were similar. The X-ray diffractograms of the calcined catalysts only contained reflections characteristic for tetragonal  $Ce_{13}Zr_{0.87}O_2$  (ICDD 04-026-5667), which may suggest that the metals were well dispersed before the reduction (Fig. S1, Supplementary Materials) [36].

The Lewis acid site concentration of the catalysts was higher compared to the bare  $CeO_2$ - $ZrO_2$  support, except in the case of Pt and Ru (Table 1). Particularly the presence of Ni and Cu increased the Lewis acid site concentration. Fig. S2 of the Supplementary Materials displays the FTIR spectra of the pyridine saturated catalysts. No major shifts were observed for the location of the vibration bands characteristic for pyridine adsorbed on Lewis acid sites ( $\sim 1442\text{ cm}^{-1}$ ) which indicates that

the Lewis acid site strength of the catalysts was similar (Table S1, Supplementary Materials). Brønsted acid sites were only detected on the Ni-containing catalysts (15–30  $\mu\text{mol/g}$ ). The weak Lewis acid sites on the  $CeO_2$ - $ZrO_2$  support catalyze the initial conversion of primary amides via bimolecular deammoniation, promote the conversion of primary amides via hemiaminal routes, and enhance the activity for HDO of the oxygen-containing intermediate products in the reaction network, as elaborated previously by Verkama et al. [7].

The studied catalysts exhibited a higher concentration of basic sites than the  $CeO_2$ - $ZrO_2$  support (Table 1). The  $CO_2$  desorption profiles are presented in Fig. 1. The  $CO_2$ -TPD profiles of the samples contained a

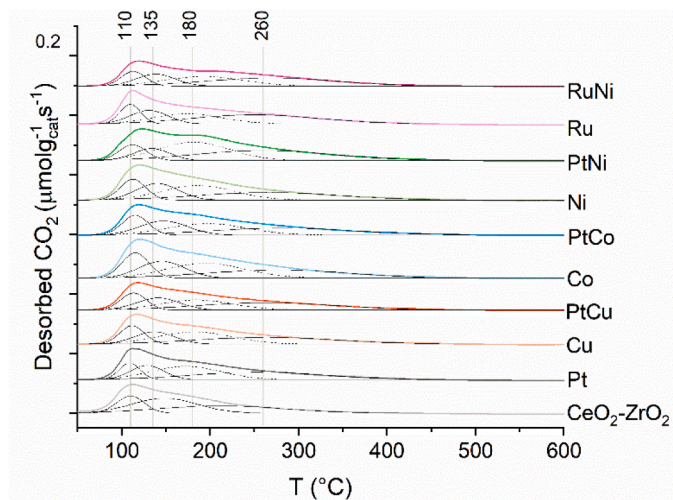


Fig. 1.  $CO_2$ -TPD profiles of the catalysts and the  $CeO_2$ - $ZrO_2$  support. The samples were reduced in  $H_2$  at 350 °C before the  $CO_2$ -TPD measurements.

Table 1

Catalyst properties based on characterization via semi-quantitative XRF,  $N_2$ -physisorption, CO pulse titration,  $CO_2$ -TPD and pyridine FTIR measurements.

Catalyst	Metal loading		$N_2$ -Physisorption <sup>a</sup>			CO adsorption <sup>b</sup> ( $\mu\text{mol/g}_{\text{cat}}$ )	$CO_2$ -TPD and pyridine FTIR		
	Target (wt %)	Semi-quantitative XRF <sup>a</sup> (wt%)	$S_{\text{BET}}$ ( $m^2/g_{\text{cat}}$ )	$V_{\text{pore}}$ ( $cm^3/g_{\text{cat}}$ )	$d_{\text{pore, mean}}$ (nm)		Total basicity <sup>b,c</sup> ( $\mu\text{mol/g}_{\text{cat}}$ )	BAS <sup>d</sup> ( $\mu\text{mol/g}_{\text{cat}}$ )	LAS <sup>e</sup> ( $\mu\text{mol/g}_{\text{cat}}$ )
$CeO_2$ - $ZrO_2$	-	-	87	0.19	8.2	-	130	-	60
Pt	0.5 wt% Pt	0.3 wt% Pt	85	0.21	7.9	16	160	-	40
Ru	0.5 wt% Ru	1.0 wt% Ru	87	0.20	8.1	78	170	-	50
Ni	1.5 wt% Ni	1.2 wt% Ni	78	0.19	8.1	8	200	15	140
Co	1.5 wt% Co	1.2 wt% Co	83	0.18	8.1	-	220	-	80
Cu	1.5 wt% Cu	1.1 wt% Cu	83	0.20	8.1	-	170	-	250
RuNi	0.5 wt% Ru 1.5 wt% Ni	0.8 wt% Ru 1.1 wt% Ni	81	0.18	8.5	148	160	30	160
PtNi	0.5 wt% Pt 1.5 wt% Ni	0.3 wt% Pt 1.2 wt% Ni	81	0.17	8.3	60	210	15	130
PtCo	0.5 wt% Pt 1.5 wt% Co	0.3 wt% Pt 1.2 wt% Co	88	0.21	7.8	24	180	-	90
PtCu	0.5 wt% Pt 1.5 wt% Cu	0.3 wt% Pt 1.2 wt% Cu	83	0.20	7.9	15	160	-	220

<sup>a</sup> The analysis was carried out for the calcined catalysts.

<sup>b</sup> The samples were reduced in  $H_2$  at 350 °C before the measurements.

<sup>c</sup> Amount of desorbed  $CO_2$  from  $CO_2$ -TPD.

<sup>d</sup> Pyridine adsorbed on Brønsted acid sites ( $1550\text{ cm}^{-1}$ ).

<sup>e</sup> Pyridine adsorbed on Lewis acid sites ( $1442\text{ cm}^{-1}$ ).

broad peak between approximately 70 and 450 °C, which is likely related to the desorption of CO<sub>2</sub> that had been adsorbed on Lewis basic sites, Brønsted basic sites and on Lewis acid–basic site pairs [37,38]. The CO<sub>2</sub> desorption peak of the catalysts could be deconvoluted using four Gaussian components centered at 109–115 °C, 130–147 °C, 172–196 °C and 253–276 °C (Table S2, Supplementary Materials). The CO<sub>2</sub> desorption peak of the bare CeO<sub>2</sub>-ZrO<sub>2</sub> support, in turn, was deconvoluted with three Gaussian components centered at 110 °C, 149 °C and 212 °C. Considering the higher desorption temperature, the CO<sub>2</sub> adsorption was somewhat stronger on the metal catalysts than on the bare support, but the adsorption strength also differed between the catalysts (Table S2, Supplementary Materials). The PtNi, Ni and Co catalysts had the highest concentration of the strong Lewis or Brønsted basic sites, or Lewis acid–basic site pairs. The CO<sub>2</sub> desorption peak of the measurement on the RuNi catalyst was also shifted to a relatively high temperature, as indicated by the location of the Gaussian components that were used to deconvolute the data (113, 138, 193 and 269 °C).

The reducibility of the calcined catalysts was qualitatively studied through H<sub>2</sub>-TPR measurements. The H<sub>2</sub>-TPR profiles of the bimetallic catalysts deviated from the superposition of the H<sub>2</sub>-TPR profiles of the corresponding monometallic catalysts, as seen from Fig. 2. The noble metals (Pt, Ru) enhanced the reducibility of the base metals (Co, Ni, Cu), potentially due to hydrogen spillover or alloy formation [17,18,24]. Based on the H<sub>2</sub>-TPR profiles of the bimetallic catalysts, it is possible that the base metals delayed the reduction of the noble metals. This might be related to interactions between the metals or an enhanced interaction between the noble metal and the support [17,18]. Alternatively, this could reflect competitive adsorption of the metals to the support during the catalyst preparation [17,18]. The bare CeO<sub>2</sub>-ZrO<sub>2</sub> support exhibited a reduction peak at 550 °C, likely attributed to the reduction of Ce<sup>4+</sup> to Ce<sup>3+</sup> [39,40]. The active metals lowered the reduction temperature of the CeO<sub>2</sub>-ZrO<sub>2</sub> support and the reduction of the support may have occurred concurrently with the metals [39,40]. The peaks of the reduction profiles could therefore not be reliably assigned to specific metal species. In the case of the monometallic Pt catalyst, the reduction peak at approximately 325 °C is most likely related to the Pt-assisted reduction of CeO<sub>2</sub> [7,39,40]. The H<sub>2</sub>-TPR profiles of the monometallic Ni and Co catalysts showed broad reduction peaks between approximately 150 and 450 °C, likely indicative of strong interactions between the Ni and Co oxides and the CeO<sub>2</sub>-ZrO<sub>2</sub> support. It is therefore possible, that Ni and Co oxides were present on the monometallic Ni and Co catalysts after the reduction treatment that was used for the activity tests (350 °C, 20 bar H<sub>2</sub>). Otherwise, the H<sub>2</sub>-TPR measurements suggested that the active metals were in their metallic state in the activity tests.

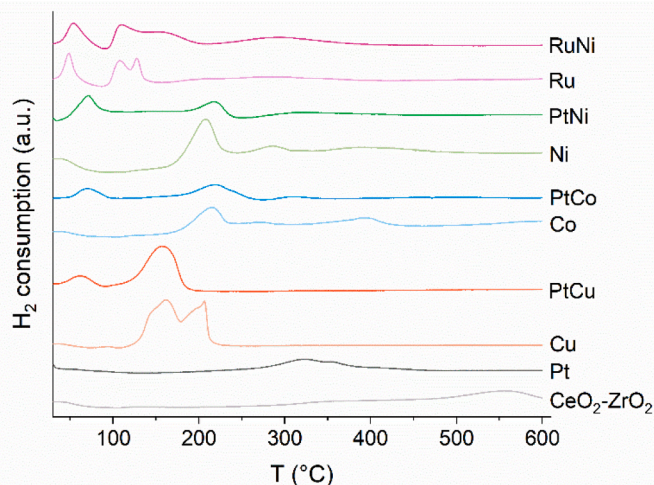


Fig. 2. H<sub>2</sub>-TPR profiles of the calcined catalysts and the CeO<sub>2</sub>-ZrO<sub>2</sub> support.

A selection of HAADF-STEM images with elemental EDS mappings is presented in Fig. 3. The analysis was carried out for the calcined catalysts. It was hard to reliably estimate the particle size distribution due to the weak contrast between the active metals and the CeO<sub>2</sub>-ZrO<sub>2</sub> support. However, relatively large Co clusters (>15 nm) were clearly displayed in the elemental EDS mappings of the Co-containing catalysts, whereas the Ni appeared to be moderately better dispersed.

As seen from Table 1, the CO adsorption capacity of the bimetallic RuNi (148 μmol/g<sub>cat</sub>) and PtNi (60 μmol/g<sub>cat</sub>) catalysts considerably exceeded the CO adsorption capacity of the monometallic Ni (8 μmol/g<sub>cat</sub>), Ru (78 μmol/g<sub>cat</sub>) and Pt (16 μmol/g<sub>cat</sub>) catalysts. The increased CO adsorption capacity of the bimetallic catalysts may hint towards an increased metal dispersion, or reflect the increased reducibility of Ni (Fig. 2) [17,18]. However, as the adsorption stoichiometry of CO on the metals likely differed, the CO adsorption capacity should not be taken as a direct measure of the number of surface metal sites. The CO adsorption capacity of the monometallic Co catalyst was negligible, whereas the bimetallic PtCo catalyst (24 μmol/g<sub>cat</sub>) only adsorbed slightly more CO compared to the monometallic Pt catalyst. This may suggest that the Co dispersion was poor, as could be expected from the STEM-EDS analysis of the calcined catalysts (Fig. 3), where large Co clusters were observed on both Co and PtCo [41]. Considering the relatively high reduction temperature (Fig. 2), it is also possible that the negligible CO adsorption capacity of the monometallic Co catalyst partly reflected an incomplete reduction of Co. However, the adsorption stoichiometry of CO on Co varies depending on the catalyst composition, which brings further uncertainty to the analysis [42,43]. Low Co dispersions are often encountered in catalysts prepared by incipient wetness impregnation [41–43]. As reduced Cu does not chemisorb CO, the similar CO adsorption capacity of PtCu (15 μmol/g<sub>cat</sub>) and the monometallic Pt suggests that the Pt dispersion was not affected by Cu [44].

XPS measurements were carried out to study the chemical state of the catalyst surface. The samples were reduced ex-situ in H<sub>2</sub> at 350 °C for 60 min and transferred to the equipment in atmosphere. The survey spectra and high-resolution spectra are available in the Supplementary Materials (Fig. S3, Fig. S4). Table 2 presents the active metal surface concentration, atomic ratio of the active metals calculated from the surface composition and from the nominal loadings, and the atomic ratio of active metal to the total amount of Ce and Zr on the catalyst surface. Table 2 additionally displays the amount of cerium as Ce<sup>3+</sup> and the amount Zr in a higher binding energy state compared to ZrO<sub>2</sub>, relative to the total amounts of Ce and Zr, respectively. The share of surface O as OH species is included as well.

The co-impregnation decreased the surface concentration of Pt by 1/3–1/2, but increased the surface concentration of the base metals by a factor of 4–7 compared to the monometallic catalysts (Table 2), even though the bulk metal loadings were comparable for the bimetallic and monometallic catalysts (Table 1). In the case of RuNi, the surface concentration of Ru and Ni did not markedly change from the monometallic catalysts. The atomic ratio between the noble metal and the base metal was 5–9 times higher on the surface compared to the nominal bulk ratio, reflecting the relative enrichment of Pt and Ru on the surface of the catalysts. The atomic ratio of active metal(s) to the sum of Ce and Zr was considerably higher on the surface of the Pt-containing catalysts than on the other samples.

The XPS analysis indicated that the majority (63–75%) of the Pt on the surface was metallic, while the other metals were mainly oxidic (Table S2, Supplementary Materials). Surface oxidation may have occurred during the exposure to atmosphere during the sample transfer to the equipment, particularly in the case of the base metals (Fig. 2) [20, 22]. The H<sub>2</sub>-TPR measurements are therefore more reliable for the assessment of the reducibility of the active metals. Approximately 40% of the surface Ce atoms of the CeO<sub>2</sub>-ZrO<sub>2</sub> support were present as Ce<sup>3+</sup> on most catalysts, with Pt (51%) and PtCo (32%) deviating from the other materials slightly. The highest amounts (22–32%) of Zr in the higher binding energy state compared to ZrO<sub>2</sub> were found on Co, Ni,

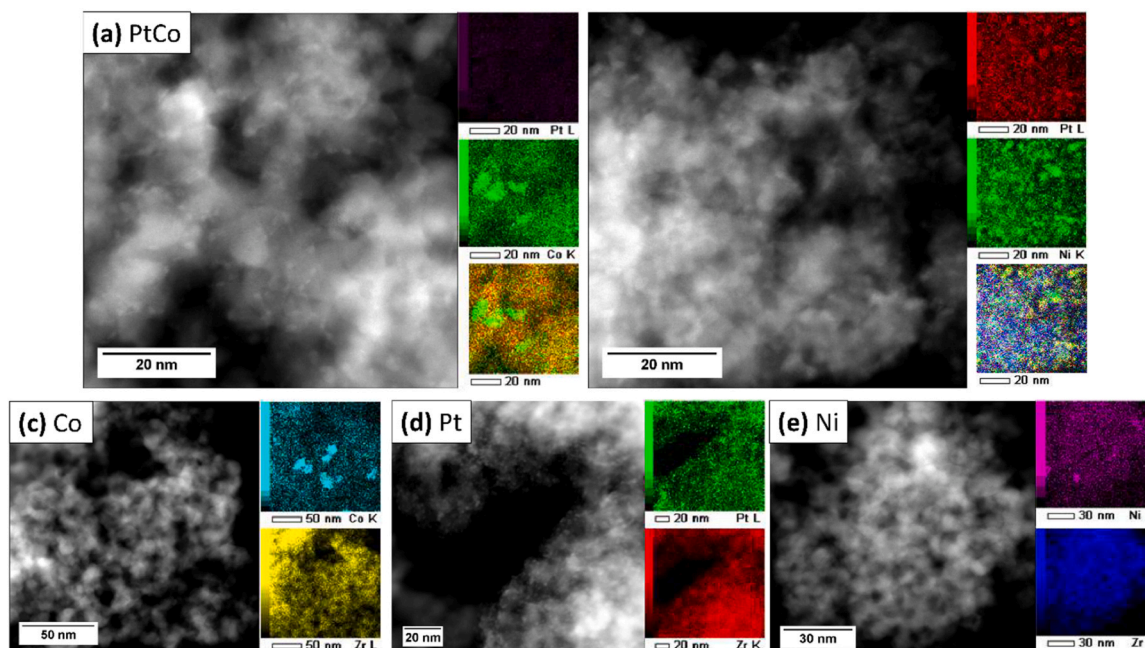


**Fig. 3.** STEM-HAADF images and corresponding EDS mappings of the calcined (a) PtCo, (b) PtNi, (c) Co, (d) Pt and (e) Ni catalysts. Note that the images differ in scale.

**Table 2**

The XPS-derived surface concentration of active metal, atomic ratio of the active metals on the surface, the nominal atomic bulk ratio of the metals, the ratio of active metals to Ce and Zr, and the relative amounts of Ce as  $\text{Ce}^{3+}$  and Zr in the higher binding energy state, and of O as OH species.  $M_1 = \text{Pt}$  or Ru,  $M_2 = \text{Ni}$ , Co or Cu.

Catalyst <sup>a</sup>	Surface concentration of $M_1$ and $M_2$ (at %) <sup>b</sup>	$M_1/M_2$ ratio, XPS	$M_1/M_2$ ratio, nominal	$(M_1 + M_2) / (\text{Ce} + \text{Zr})$	$\text{Ce}^{3+} / \text{Ce}_{\text{tot}}$ (%)	$\text{Zr}_{\text{higher B.E.}} / \text{Zr}_{\text{tot}}$ (%)	OH / $\text{O}_{\text{tot}}$ (%)
$\text{CeO}_2\text{-ZrO}_2$	-	-	-	-	37%	15%	22%
Pt	5.0 at%	-	-	0.17	51%	13%	20%
Ru	1.2 at%	-	-	0.04	40%	14%	20%
Ni	0.6 at%	-	-	0.02	39%	26%	25%
Co	0.9 at%	-	-	0.03	41%	22%	23%
Cu	0.5 at%	-	-	0.01	36%	16%	21%
RuNi	1.1 at% Ru 0.9 at% Ni	1.15	0.19	0.07	39%	32%	26%
PtNi	2.5 at% Pt 4.2 at% Ni	0.59	0.10	0.24	38%	24%	28%
PtCo	3.0 at% Pt 3.3 at% Co	0.91	0.10	0.24	32%	16%	24%
PtCu	2.0 at% Pt 3.4 at% Cu	0.59	0.11	0.19	43%	14%	22%

<sup>a</sup> The samples were reduced ex-situ in  $\text{H}_2$  at 350 °C before the measurements and transferred to the equipment through air.

<sup>b</sup> Includes adventitious carbon contamination.

PtNi and RuNi. The higher binding energy state component of Zr may be related to, e.g., the surface OH groups and other defects. The Ni, PtNi and RuNi catalysts likewise contained a slightly higher share of surface O in OH groups (25–28%) than the other samples.

The electron density of the active metal affects the bonding of reactants and products and can thus significantly influence the catalytic activity and selectivity [20,45,46]. The electron density of Pt, Co and Cu differed between the bimetallic and monometallic catalysts, as suggested by binding energy shifts in the XPS (Fig. S4, Supplementary Materials). This could indicate electron transfer between the active metals. Compared to the monometallic Pt catalyst (and PtCu), the Pt 4f<sub>7/2</sub> component of Pt(O) was shifted to a 0.4 and 0.2 eV higher binding energy on PtCo and PtNi, respectively. The peaks associated with CoO were shifted to a 0.3–0.4 eV lower binding energy in the Co 2p spectra of PtCo compared to the monometallic Co, while the binding energy of the peak related to CuO was 0.4 eV higher in the Cu 2p spectra of PtCu than in the Cu 2p spectra of the monometallic Cu. No significant binding

energy shifts were observed in the Ni 2p and Ru 3d spectra (Fig. S4, Supplementary Materials). However, considering the sample transfer related surface oxidation of the active metals, the uncertainty should be regarded significant (Table S2, Supplementary Materials).

### 3.2. Catalytic hydrotreatment of *n*-hexadecanamide

The product distribution of the *n*-hexadecanamide (C16 amide) hydrotreating experiments are presented in Fig. 4 for the catalysts (300 °C, 80 bar  $\text{H}_2$ , 60 min). The nitrogen removal obtained from the total nitrogen content analysis and the oxygen removal derived from the product distribution, have also been indicated in Fig. 4. The main products of the C16 amide hydrotreating experiments were *n*-pentadecane (C15 paraffin), *n*-hexadecane (C16 paraffin), *n*-hexadecanal (C16 aldehyde), 1-hexadecylamine (C16 amine), 1-hexadecanol (C16 alcohol), *n*-hexadecanitrile (C16 nitrile), palmitic acid (C16 acid), dipentadecylketone (C31 ketone), dihexadecylamine (C32 amine) and

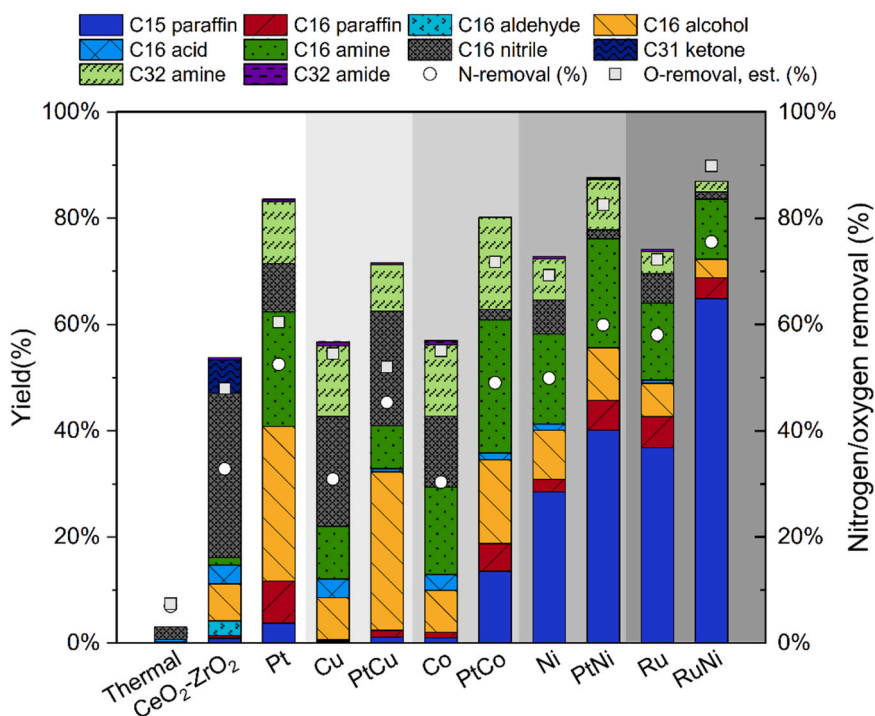


**Fig. 4.** Product distribution, nitrogen removal and oxygen removal of the C16 amide hydrotreating experiments. The nitrogen removal was obtained from the total nitrogen content analysis, while the oxygen removal was derived from the product distribution. Reaction conditions: 300 °C, 80 bar H<sub>2</sub>, 60 min, 100 ppm N.

*n*-hexadecyl hexadecanamide (C32 amide). The conversion, nitrogen removal, total paraffin yield and molar C15 to C16 paraffin ratio of the experiments are displayed in Table 3.

A proposed reaction network for the hydrotreatment of the C16 amide is presented in Scheme 1. The reaction network is based on the previous works by Verkama et al., [7,8] where the reactions and active sites have been elaborated further.

The catalysts differed from each other markedly in terms of the nitrogen removal (30–76%), oxygen removal (50–90%), paraffin yield (1–69%), C32 compound yield (2–17%) and selectivity between the C15 and C16 paraffins (0.5–16.5 mol<sub>C15 paraffin</sub>/mol<sub>C16 paraffin</sub>), as can be seen from Table 3 and Fig. 4. The RuNi, PtNi and Ru catalysts exhibited the highest nitrogen removal and paraffin yield, while the Co and Cu catalysts only were marginally more active than the bare CeO<sub>2</sub>-ZrO<sub>2</sub> support. The activity and selectivity of the bimetallic catalysts deviated from the corresponding monometallic catalysts, which is emphasized further in Fig. 5, where the product distributions of the Pt (a), PtCo (b), Co (c), Ni (d), RuNi (e), Ru (f) and PtNi (g) catalysts are presented as a function of

batch residence time. The Cu and PtCu catalysts were not studied further, as the addition of Cu impeded the hydrogenolysis and hydrogenation activity of Pt. This could be observed from the low paraffin and C16 amine yields on the PtCu catalyst. Analogous results have been reported for the hydrogenation of nitriles on Pt and PtCu catalysts [24].

Some general trends were observed in the product distribution of the CeO<sub>2</sub>-ZrO<sub>2</sub> supported catalysts (Fig. 4). The support influenced the initial C16 amide conversion route, as can be seen from the similar yields of oxygen-containing and nitrogen-containing intermediate products in the product samples of the catalysts at the first batch residence time points (Fig. 5) [7]. The active metal(s) determined the activity and selectivity for the further conversion of the intermediate products via condensation reactions and the C–C, C–O and C–N bond cleavage routes, as reflected by significant variation in the yields of the C32 amine, the C15 paraffin and the C16 paraffin [8]. HDO proceeded more efficiently than HDN, and the C16 and C32 amines were the last intermediate products to be converted on the studied catalysts, regardless of the overall activity. The following paragraphs discuss the activity and product distribution of the different monometallic and bimetallic catalysts.

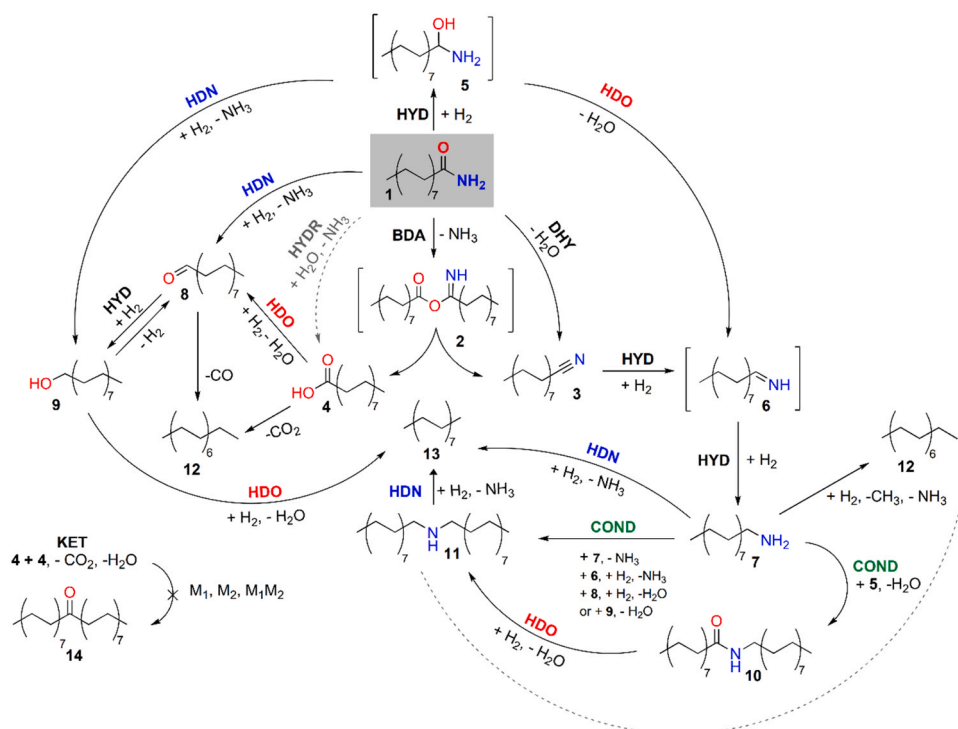
The monometallic Pt catalyst favored the formation of the C16 paraffin via HDO of the C16 alcohol and HDN of the C16 and C32 amines (Scheme 1, Fig. 4, Fig. 5a), as elaborated previously [7]. The low-activity monometallic Co catalyst only produced traces of the paraffins and strongly favored the formation of the C32 amine (Fig. 5c). Consequently, the maximum C32 amine yield of the monometallic Co catalyst (54%) was almost 30 percentage points higher than on the other studied catalysts.

Similarly to the monometallic Pt catalyst, PtCo gave significant intermediate yields (>20%) of the C16 alcohol, C16 amine and C32 amine (Fig. 5b). However, PtCo was more selective for the formation of the C15 paraffin than the C16 paraffin, which indicates that PtCo could catalyze the conversion of the C16 alcohol, C16 amine and possibly the C32 amine to the C15 paraffin. The conversion of the C16 alcohol to the C15 paraffin may have proceeded via dehydrogenation of the C16 alcohol to the C16 aldehyde on the metal sites, followed by decarbonylation to the

**Table 3**  
Conversion, nitrogen removal, total paraffin yield, total C32 compound yield and molar C15 to C16 paraffin ratio of the catalysts (300 °C, 80 bar H<sub>2</sub>, 60 min).

Catalyst	Conversion (%)	Nitrogen removal (%)	Paraffin yield (%)	C32 compound yield (%)	C15 to C16 paraffin ratio (mol/mol)
CeO <sub>2</sub> -ZrO <sub>2</sub>	69%	33%	1%	< 1% <sup>a</sup>	1.9
Pt	90%	52%	12%	12%	0.5
Ru	80%	58%	43%	5%	6.3
Ni	81%	50%	31%	8%	12.3
Co	69%	30%	2%	14%	1.0
Cu	70%	31%	1%	14%	1.0
RuNi	93%	76%	69%	2%	16.5
PtNi	92%	60%	46%	10%	7.2
PtCo	90%	49%	19%	17%	2.6
PtCu	83%	45%	2%	9%	0.8

<sup>a</sup> Product sample contained 6% of the C31 ketone.



**Scheme 1.** Proposed reaction network for the hydrotreatment of *n*-hexadecanamide (C16 amide). Indicated compounds: 1 C16 amide, 2 C32 isoimide, 3 C16 nitrile, 4 C16 acid, 5 C16 hemiaminal, 6 C16 imine, 7 C16 amine, 8 C16 aldehyde, 9 C16 alcohol, 10 C32 amide, 11 C32 amine, 12 C15 paraffin, 13 C16 paraffin, 14 C31 ketone. The bimolecular deamination (BDA), direct dehydration (DHY), hydrogenation (HYD) and hydrolysis (HYDR) of the C16 amide, and the condensation (COND), hydrodeoxygenation (HDO) and hydrodenitrogenation (HDN) reactions of the intermediates have been indicated. The bimolecular ketonization of the C16 acid (KET) only occurred on the bare CeO<sub>2</sub>-ZrO<sub>2</sub> support. Note that the C15 paraffin (12) is indicated twice in the reaction network. The reaction network has been adapted from a previous work by Verkama et al. [7] with permission from the Royal Society of Chemistry.

C15 paraffin (Scheme 1) [47]. Some C16 paraffin was formed on PtCo as well. PtCo also exhibited a higher activity for the hydrogenation of the C16 nitrile to the C16 amine than the monometallic Pt and Co catalysts. It is possible that the enhanced C–C bond cleavage and nitrile hydrogenation activity of PtCo were a consequence of the electronic interactions between the active metals, which could be observed from the decreased electron density of Pt and increased electron density of Co in the XPS analysis (Fig. S4, Supplementary Materials) [18,24,45,48,49]. Nevertheless, the total paraffin yield of PtCo did not exceed the total paraffin yield of the monometallic Pt catalyst at batch residence times above 0.75 g<sub>cat</sub>h/g<sub>amide</sub>.

The monometallic Ni catalyst formed the C15 paraffin via C–C bond cleavage of C16 alcohol and the C16 amine intermediates (Fig. 5d). Furthermore, the decomposition of the C32 amine on the Ni catalyst was accompanied by an increase in the C15 paraffin yield, while the yields of the other compounds either decreased, or in the case of the C16 paraffin, remained stable. The monometallic Ni catalyst therefore appeared to show activity for the conversion of the C32 amine to the C15 paraffin, but the conversion route could not be deduced from the experimental data. The decomposition of the C32 amine to the C15 paraffin was likewise observed on the PtNi catalyst (Fig. 5g).

The activity of PtNi exceeded the activity of the monometallic Pt and Ni catalysts (Fig. 4, Fig. 5). The product distribution of PtNi resembled the monometallic Ni more than Pt, which might be related to nickel-rich surface (Table 2). The relatively high yields of the C16 amine and C16 alcohol at batch residence times below 1 g<sub>cat</sub>h/g<sub>amide</sub> suggest that the PtNi catalyst favored the initial conversion of the C16 amide via the hemiaminal routes and BDA. The high hydrogenation activity of PtNi may have facilitated the formation of the hemiaminal intermediate [50]. PtNi catalysts have been proposed to catalyze HDO reactions via a bifunctional mechanism involving the hydrogenation of reaction intermediates on Pt sites followed by hydrogenolysis on Ni sites [26,51],

and an analogous synergy between Pt and Ni could be possible in the hydrotreatment of the C16 amide. As with PtCo, electronic interactions between Pt and Ni (Fig. 2 and Fig. S4, Supplementary Materials) may have further contributed towards the enhanced C–C bond cleavage activity of the PtNi catalyst [45,48].

The monometallic Ru and bimetallic RuNi catalysts were highly active and selective for the formation of the C15 paraffin (Fig. 4, Fig. 5). The activity of the monometallic Ru catalyst was similar to PtNi, while RuNi exhibited the highest activity for the formation of the C15 paraffin out of all studied catalysts. At a reaction time of 60 min, the paraffin yield and nitrogen removal of RuNi were 26% and 18 percentage points higher, respectively, compared to the monometallic Ru catalyst (Table 3). Less C16 compounds and less C32 amine were present in the product samples of Ru and RuNi compared to the other catalysts, indicating that these products were not formed or that Ru and RuNi were highly active for their conversion to the C15 paraffin (Fig. 5d-f). It is possible that a direct C–C bond cleavage route of the C16 amide was favored on the Ru and RuNi catalysts. Out of the intermediate products, the C16 amine was present in the highest concentration, with a maximum yield of 15%. In a previous work by Verkama et al., [8] the formation of the C32 amine was suppressed on Ru/ZrO<sub>2</sub> and favored on Pt/ZrO<sub>2</sub> and Ni/ZrO<sub>2</sub>. The relatively low C32 amine yield on the monometallic Ru/CeO<sub>2</sub>-ZrO<sub>2</sub> catalyst (<9%) was therefore expected. The C32 amine yield on the RuNi/CeO<sub>2</sub>-ZrO<sub>2</sub> catalyst (<2%) was the lowest out of all studied catalysts, which is remarkable considering the significant C32 amine yield on the monometallic Ni/CeO<sub>2</sub>-ZrO<sub>2</sub> catalyst (≈20%).

From the nitrogen removal, oxygen removal and product distribution of the RuNi catalyst (Fig. 4), it is evident that doping with Ni enhanced the hydrogenolysis activity compared to the Ru catalyst. The product distribution of RuNi resembled the monometallic Ru catalyst more than the monometallic Ni catalyst due to the low yields of the oxygen-

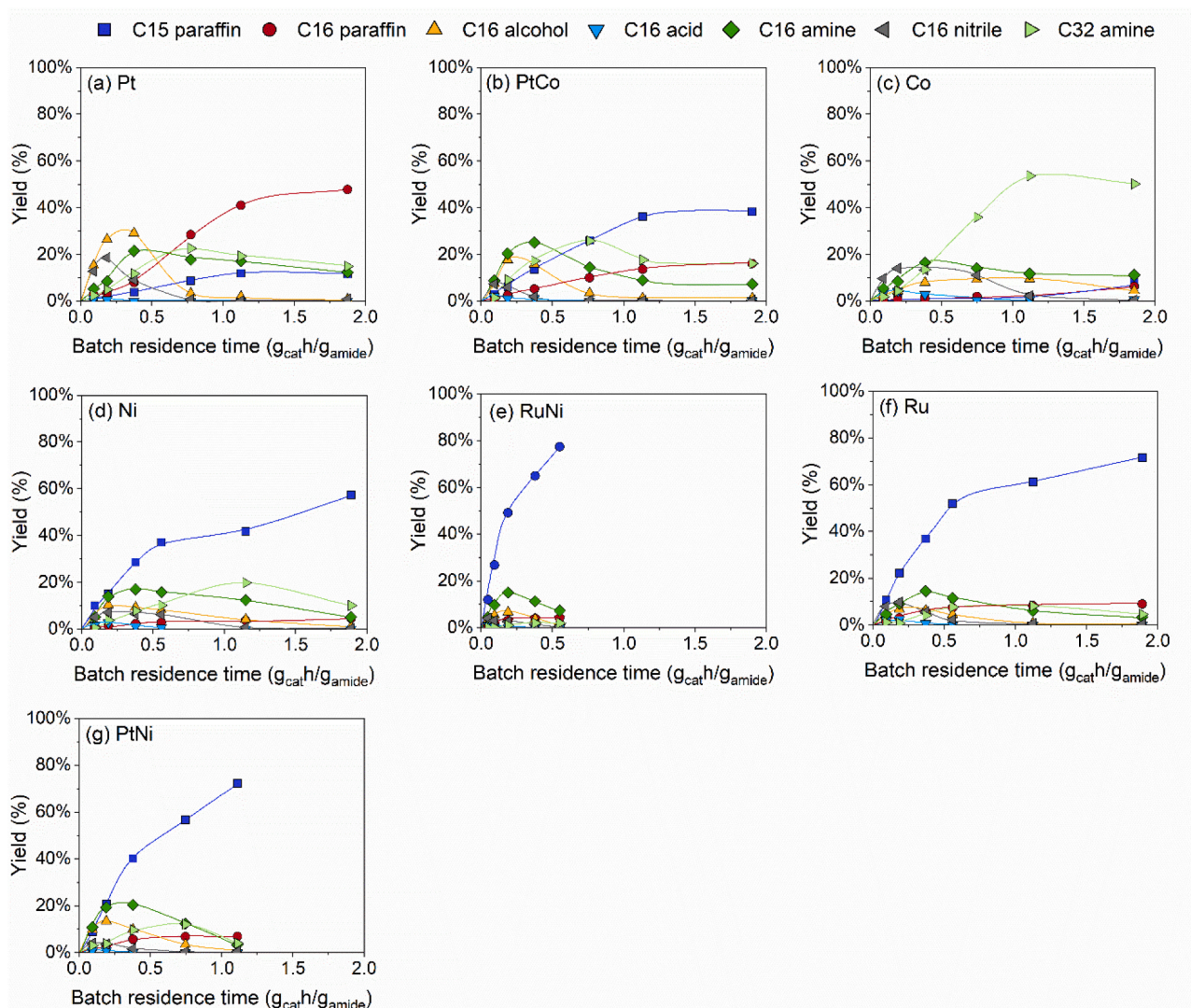


Fig. 5. Product distribution for the hydrotreatment of the C16 amide at 300 °C and 80 bar H<sub>2</sub> as a function of batch residence time for the CeO<sub>2</sub>-ZrO<sub>2</sub> supported (a) Pt, (b) PtCo, (c) Co, (d) Ni, (e) RuNi, (f) Ru and (g) PtNi catalysts. The 60 min experiments of Fig. 4 correspond to a batch residence time of 0.37 g<sub>cat</sub>h/g<sub>amide</sub>. The trendlines have been added to guide the eye.

containing and nitrogen-containing intermediate products (Fig. 5d-f), which might reflect the slightly higher concentration of Ru than Ni on the catalyst surface (Table 2). Despite the high activity, the synergistic effect between the active metals was less pronounced for RuNi compared to PtNi and PtCo, for which the monometallic catalysts exhibited markedly different product distributions. The enhanced hydrogenolysis activity of bimetallic RuNi catalysts has been suggested to stem from electronic interactions between the metals, which promotes the activation of reactants and hydrogen [20,21].

As discussed above, the catalytic properties of the bimetallic catalysts differed from the corresponding monometallic catalysts, with the combination of Ni with Pt and Ru emerging as particularly active for the hydrotreatment of the C16 amide (Fig. 4, Fig. 5). Interactions between the active metals, as indicated by the H<sub>2</sub>-TPR and XPS analysis, provide one reason for the observed differences in the activity and selectivity. Furthermore, the CO adsorption capacity and Lewis acid site concentration of the catalysts emerged as important properties, as illustrated in Fig. 6.

There was a positive correlation between the total paraffin yield and the CO adsorption capacity (Fig. 6a), and between the total paraffin yield and the Lewis acid site concentration of the catalysts (Fig. 6b). Both metal sites and Lewis acid sites of the support are mechanistically

involved in the hydrogenolysis mechanisms, and the Lewis acid sites that are located near the perimeter of the metal particles have been proposed to be critical for the activity [12,45,53,54]. The enhanced hydrogenolysis activity of the RuNi and PtNi catalysts can thus also be related to the increased number of surface metal sites and Lewis acid sites compared to the monometallic counterparts. Meanwhile, the relatively low activity of the PtCo catalyst may be due to a lower concentration of surface metal sites and Lewis acid sites. The Cu and PtCu catalysts deviated from the trend due to the poor hydrogenolysis activity of Cu, which may be related to the weak adsorption of the intermediate products on Cu sites [24,55].

The nitrogen removal increased with an increasing CO adsorption capacity (Fig. 6c), but there was no significant correlation between the Lewis acid site concentration and nitrogen removal (Fig. 6d). While metal sites are required for the formation of paraffins, the CeO<sub>2</sub>-ZrO<sub>2</sub> support removed nitrogen on its own via bimolecular deamination of the C16 amide (Scheme 1), which accounts for the higher nitrogen removal than paraffin yield on the studied catalysts (Table 3) [7,52].

It cannot be excluded that the Brønsted acid sites on PtNi and RuNi (Table 1) further enhanced the dehydration, HDO and HDN activity of the catalysts [4,10,47]. It is also possible that the strong basic sites on the Ni-containing catalysts (Fig. 1) contributed to their activity,

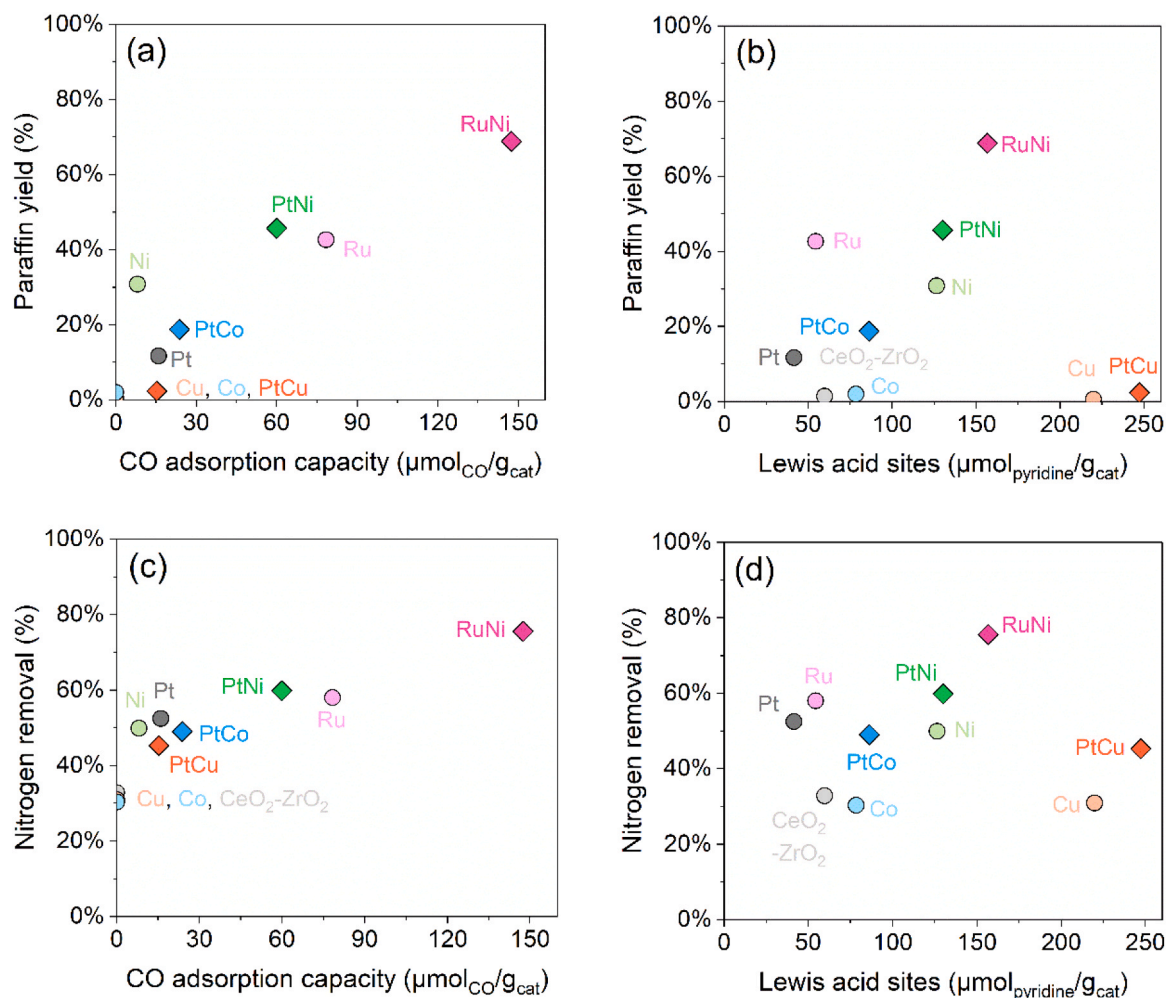


**Fig. 6.** Combined yield of the C15 paraffin and C16 paraffin in the hydrotreatment of the C16 amide as a function of the (a) CO adsorption capacity and (b) Lewis acid site concentration, and the nitrogen removal in the hydrotreatment of the C16 amide as a function of the (c) CO adsorption capacity and (d) Lewis acid site concentration. Reaction conditions: 300 °C, 80 bar H<sub>2</sub>, 60 min.

considering that strong Lewis basic sites have been proposed to benefit HDO activity by facilitating the adsorption of carbonyl compounds [10, 56]. The differences in the reducibility of the CeO<sub>2</sub>-ZrO<sub>2</sub> support were relatively small between the catalysts (Table 2) and did not account for the differences in the catalytic activity.

#### 4. Conclusions

The HDO and HDN of the C16 amide (*n*-hexadecanamide) was studied on Pt, Co, PtCo, Cu, PtCu, Ni, PtNi, Ru and RuNi catalysts supported on CeO<sub>2</sub>-ZrO<sub>2</sub>. The studied bimetallic catalysts exhibited synergistic effects between the active metals, which could be observed from differences in the activity and selectivity compared to the corresponding monometallic catalysts (Figs. 4–6). Catalyst characterization via H<sub>2</sub>-TPR, XPS and CO pulse titration measurements likewise indicated interactions between the active metals.

The PtCo catalyst clearly deviated from the monometallic Pt and Co catalysts by favoring the formation of the C15 paraffin, compared to the formation of the C16 paraffin on the monometallic Pt and the C32 amine on the monometallic Co. Characterization by XPS suggested that the selectivity of PtCo may have been related to electronic interactions between Pt and Co. Despite a different selectivity, PtCo was not markedly more active than the monometallic Pt catalyst, which may have been due to a small difference in their number of surface metal sites. The addition of Cu impeded the hydrogenation and hydrogenolysis activity

of Pt. Consequently, the PtCu catalyst exhibited a lower activity and paraffin yield than the monometallic Pt catalyst.

The combination of Ni with Ru and Pt was found to be particularly beneficial for the catalytic activity, and the RuNi and PtNi catalysts exhibited a high activity and selectivity for the formation of the C15 paraffin via C–C bond cleavage routes. The activity of the RuNi and PtNi catalysts may have been due to electronic interactions between the metals and an increased number of surface metal sites and Lewis acid sites. Overall, this work emphasized the potential of bimetallic catalysts for the simultaneous HDO and HDN of renewable feedstocks to fuels.

#### CRedit authorship contribution statement

**Emma Verkama:** Writing – original draft, Visualization, Methodology, Investigation, Formal analysis, Conceptualization. **Ellen Järvinen:** Investigation. **Sylvia Albersberger:** Writing – review & editing, Project administration, Conceptualization. **Kristoffer Meinander:** Writing – review & editing, Investigation, Formal analysis. **Hua Jiang:** Writing – review & editing, Investigation. **Marja Tiitta:** Writing – review & editing, Supervision, Conceptualization. **Reetta Karinen:** Writing – review & editing, Supervision, Conceptualization. **Riikka L. Puurunen:** Writing – review & editing, Supervision, Project administration, Funding acquisition, Conceptualization.

## Declaration of Competing Interest

Non-disclosure agreement prevents researchers from disclosing conflict of interest.

## Data availability

The data that has been used is confidential.

## Acknowledgements

The Bioeconomy and Raw materials research infrastructures at Aalto University and the OtaNano Nanomicroscopy center were used in this work. Dr. Yingnan Zhao and the Research Analytics department of Neste Corporation are acknowledged for the equipment support and guidance with the acid site characterization. This work was funded by Neste Corporation (Neste-Aalto HDN catalyst development project).

## Appendix A. Supporting information

Supplementary data associated with this article can be found in the online version at [doi:10.1016/j.apcata.2024.119602](https://doi.org/10.1016/j.apcata.2024.119602).

## References

- [1] O. Palardy, C. Behnke, L.M.L. Laurens, *Energy Fuels* 31 (2017) 8275–8282, <https://doi.org/10.1021/acs.energyfuels.7b01175>.
- [2] T. Madl, M. Mittelbach, *Analyst* 130 (2005) 565–570, <https://doi.org/10.1039/b415779f>.
- [3] E. Verkama, P. Auvinen, S. Albersberger, M. Tiitta, R. Karinen, R.L. Puurunen, *Top. Catal.* 66 (2023) 1353–1368, <https://doi.org/10.1007/s11244-023-01784-w>.
- [4] M. Liu, Y. Shi, K. Wu, J. Liang, Y. Wu, S. Huang, M. Yang, *Catal. Commun.* 129 (2019) 105726, <https://doi.org/10.1016/j.catcom.2019.105726>.
- [5] J. Liang, R. Ding, Y. Wu, Y. Chen, K. Wu, Y. Meng, M. Yang, Y. Wang, *J. Mol. Catal. A: Chem.* 411 (2016) 95–102, <https://doi.org/10.1016/j.molcata.2015.10.018>.
- [6] C. Zhu, O.Y. Gutiérrez, D.M. Santosa, M. Flake, R. Weindl, I. Kutnyakov, H. Shi, H. Wang, *Appl. Catal. B: Environ.* 307 (2022) 121197, <https://doi.org/10.1016/j.apcatb.2022.121197>.
- [7] E. Verkama, S. Albersberger, A. Arandia, K. Meinander, M. Tiitta, R. Karinen, R. L. Puurunen, *Catal. Sci. Technol.* 14 (2024) 431–448, <https://doi.org/10.1039/D3CY01480K>.
- [8] E. Verkama, S. Albersberger, K. Meinander, M. Tiitta, R. Karinen, R.L. Puurunen, *Energy Fuels* (2024), <https://doi.org/10.1021/acs.energyfuels.3c04372> in press.
- [9] K. Malins, *Fuel* 285 (2021) 119129, <https://doi.org/10.1016/j.fuel.2020.119129>.
- [10] S. Ding, C.M.A. Parlett, X. Fan, *Mol. Catal.* 523 (2021) 111492, <https://doi.org/10.1016/j.mcat.2021.111492>.
- [11] M. Snåre, I. Kubičková, P. Mäki-Arvela, K. Eränen, D.Yu Murzin, *Ind. Eng. Chem. Res.* 45 (2006) 5708–5715, <https://doi.org/10.1021/ie060334i>.
- [12] K. Kon, W. Onodera, S. Takakusagi, K. Shimizu, *Catal. Sci. Technol.* 4 (2014) 3705–3712, <https://doi.org/10.1039/C4CY00757C>.
- [13] W. Yu, M.D. Porosoff, J.G. Chen, *Chem. Rev.* 112 (2012) 5780–5817, <https://doi.org/10.1021/cr300096b>.
- [14] D.M. Alonso, S.G. Wettstein, J.A. Dumesic, *Chem. Soc. Rev.* 41 (2012) 8075–8098, <https://doi.org/10.1039/C2CS35188A>.
- [15] L. Liu, A. Corma, *Chem. Rev.* 123 (2023) 4855–4933, <https://doi.org/10.1021/acs.chemrev.2c00733>.
- [16] J.H. Sinfelt, *Acc. Chem. Res.* 10 (1977) 15–20, <https://doi.org/10.1021/ar50109a003>.
- [17] O.U. Valdés-Martínez, V.A. Suárez-Toriello, J.A. de los Reyes, B. Pawelec, J.L. G. Fierro, *Catal. Today* 296 (2017) 219–227, <https://doi.org/10.1016/j.cattod.2017.04.007>.
- [18] P.T.M. Do, A.J. Foster, J. Chen, R.F. Lobo, *Green. Chem.* 14 (2012) 1388–1397, <https://doi.org/10.1039/C2GC16544A>.
- [19] R. Rios-Escobedo, E. Ortiz-Santos, J.A. Colín-Luna, J.N. Díaz de León, P. del Angel, J. Escobar, J.A. de los Reyes, *Top. Catal.* 65 (2022) 1448–1461, <https://doi.org/10.1007/s11244-022-01662-x>.
- [20] R. Li, J. Qiu, H. Chen, R. Shu, Y. Chen, Y. Liu, P.-F. Liu, *Fuel* 281 (2020) 118758, <https://doi.org/10.1016/j.fuel.2020.118758>.
- [21] J. Zhang, J. Teo, X. Chen, H. Asakura, T. Tanaka, K. Teramura, N. Yan, *ACS Catal.* 4 (2014) 1574–1583, <https://doi.org/10.1021/cs401199f>.
- [22] J. Zhang, K. Sun, D. Li, T. Deng, G. Lu, C. Cai, *Appl. Catal. A: Gen.* 569 (2019) 190–195, <https://doi.org/10.1016/j.apcata.2018.10.038>.
- [23] Y. Zheng, J. Wang, D. Li, C. Liu, Y. Lu, X. Lin, Z. Zheng, *Int. J. Hydrog. Energy* 46 (2021) 27922–27940, <https://doi.org/10.1016/j.ijhydene.2021.06.082>.
- [24] Y. Huang, W.M.H. Sachtler, *J. Catal.* 188 (1999) 215–225, <https://doi.org/10.1006/jcat.1999.2645>.
- [25] C. Hirose, N. Wakasa, T. Fuchikami, *Tetrahedron Lett.* 37 (1996) 6749–6752, [https://doi.org/10.1016/S0040-4039\(96\)01458-X](https://doi.org/10.1016/S0040-4039(96)01458-X).
- [26] P. Wu, C. Cai, *Chin. Chem. Lett.* 33 (2022) 234–238, <https://doi.org/10.1016/j.ccl.2021.05.059>.
- [27] R. Burch, C. Paun, X.-M. Cao, P. Crawford, P. Goodrich, C. Hardacre, P. Hu, L. McLaughlin, J. Sá, J.M. Thompson, *J. Catal.* 283 (2011) 89–97, <https://doi.org/10.1016/j.jcat.2011.07.007>.
- [28] Y. Zhang, L. Li, F. Liu, H. Qi, L. Zhang, W. Guan, Y. Liu, A. Wang, T. Zhang, *ACS Catal.* 12 (2022) 6302–6312, <https://doi.org/10.1021/acscatal.2c01264>.
- [29] R.M. Navarro, B. Pawelec, J.M. Trejo, R. Mariscal, J.L.G. Fierro, *J. Catal.* 189 (2000) 184–194, <https://doi.org/10.1006/jcat.1999.2693>.
- [30] S. Brunauer, P.H. Emmett, E. Teller, *J. Am. Chem. Soc.* 60 (1938) 309–319, <https://doi.org/10.1021/ja01269a023>.
- [31] E.P. Barrett, L.G. Joyner, P.P. Halenda, *J. Am. Chem. Soc.* 73 (1951) 373–380, <https://doi.org/10.1021/ja01145a126>.
- [32] E. Marguif, R. Van Grieken, *X-Ray Fluorescence Spectrometry and Related Techniques: An Introduction*, Momentum Press, New York, 2013.
- [33] C.A. Emeis, *J. Catal.* 141 (1993) 347–354, <https://doi.org/10.1006/jcat.1993.1145>.
- [34] E. Bêche, P. Charvin, D. Perarnau, S. Abanades, G. Flamant, *Surf. Interface Anal.* 40 (2008) 264–267, <https://doi.org/10.1002/sia.2686>.
- [35] M.C. Biesinger, B.P. Payne, A.P. Grosvenor, L.W.M. Lau, A.R. Gerson, R.St. C. Smart, *Appl. Surf. Sci.* 257 (2011) 2717–2730, <https://doi.org/10.1016/j.apsusc.2010.10.051>.
- [36] G. Bergeret, P. Gallezot, *Handbook of Heterogeneous Catalysis*, in: *Handbook of Heterogeneous Catalysis*, John Wiley & Sons, Ltd, 2008, pp. 738–765.
- [37] X. Jia, X. Zhang, N. Rui, X. Hu, C. Liu, *Appl. Catal. B: Environ.* 244 (2019) 159–169, <https://doi.org/10.1016/j.apcatb.2018.11.024>.
- [38] T. Viinikainen, H. Rönkkönen, H. Bradshaw, H. Stephenson, S. Airaksinen, M. Reinikainen, P. Simell, O. Krause, *Appl. Catal. A: Gen.* 362 (2009) 169–177, <https://doi.org/10.1016/j.apcata.2009.04.037>.
- [39] S. Bernal, J.J. Calvino, G.A. Cifredo, A. Laachir, V. Perrichon, J.M. Herrmann, *Langmuir* 10 (1994) 717–722, <https://doi.org/10.1021/la00015a020>.
- [40] J.A. Wang, T. López, X. Bokhimi, O. Novaro, *J. Mol. Catal. A: Chem.* 239 (2005) 249–256, <https://doi.org/10.1016/j.molcata.2005.06.021>.
- [41] H. Romar, E. Rivoire, P. Tynjälä, U. Lassi, *Top. Catal.* 60 (2017) 1408–1414, <https://doi.org/10.1007/s11244-017-0822-0>.
- [42] E. Patanou, E.Z. Tveten, D. Chen, A. Holmen, E.A. Blekkan, *Catal. Today* 214 (2013) 19–24, <https://doi.org/10.1016/j.cattod.2012.12.006>.
- [43] R.C. Reuel, C.H. Bartholomew, *J. Catal.* 85 (1984) 63–77, [https://doi.org/10.1016/0021-9517\(84\)90110-6](https://doi.org/10.1016/0021-9517(84)90110-6).
- [44] E. Asedegbega-Nieto, A. Guerrero-Ruiz, I. Rodríguez-Ramos, *Thermochim. Acta* 434 (2005) 113–118, <https://doi.org/10.1016/j.tca.2005.01.026>.
- [45] J. Ni, W. Leng, J. Mao, J. Wang, J. Lin, D. Jiang, X. Li, *Appl. Catal. B: Environ.* 253 (2019) 170–178, <https://doi.org/10.1016/j.apcatb.2019.04.043>.
- [46] Y. Ji, A.M.J. Van der Eerden, V. Koot, P.J. Kooymann, J.D. Meeldijk, B. M. Weckhuysen, D.C. Koningsberger, *J. Catal.* 234 (2005) 376–384, <https://doi.org/10.1016/j.jcat.2005.06.030>.
- [47] B. Peng, C. Zhao, S. Kasakov, S. Foraita, J.A. Lercher, *Chem. Eur. J.* 19 (2013) 4732–4741, <https://doi.org/10.1002/chem.201203110>.
- [48] G.W. Huber, J.W. Shabaker, S.T. Evans, J.A. Dumesic, *Appl. Catal. B: Environ.* 62 (2006) 226–235, <https://doi.org/10.1016/j.apcatb.2005.07.010>.
- [49] W.W. Lonergan, D.G. Vlachos, J.G. Chen, *J. Catal.* 271 (2010) 239–250, <https://doi.org/10.1016/j.jcat.2010.01.019>.
- [50] J.R. Cabrero-Antonino, R. Adam, V. Papa, M. Baller, *Nat. Commun.* 11 (2020) 3893, <https://doi.org/10.1038/s41467-020-17588-5>.
- [51] L. Guo, Y. Tian, X. He, C. Qiao, G. Liu, *Fuel* 322 (2022) 124082, <https://doi.org/10.1016/j.fuel.2022.124082>.
- [52] D. Davidson, M. Kerten, *J. Am. Chem. Soc.* 78 (1956) 1066–1068, <https://doi.org/10.1021/ja01586a051>.
- [53] K.A. Resende, C.A. Teles, G. Jacobs, B.H. Davis, D.C. Cronauer, A. Jeremy Kropf, C. L. Marshall, C.E. Hori, F.B. Noronha, *Appl. Catal. B: Environ.* 232 (2018) 213–231, <https://doi.org/10.1016/j.apcatb.2018.03.041>.
- [54] C.A. Teles, P.M. de Souza, A.H. Braga, R.C. Rabelo-Neto, A. Teran, G. Jacobs, D. E. Resasco, F.B. Noronha, *Appl. Catal. B: Environ.* 249 (2019) 292–305, <https://doi.org/10.1016/j.apcatb.2019.02.077>.
- [55] A.S. Almithn, D.D. Hibbitts, *ACS Catal.* 10 (2020) 5086–5100, <https://doi.org/10.1021/acscatal.0c00481>.
- [56] J. Li, J. Zhang, S. Wang, G. Xu, H. Wang, D.G. Vlachos, *ACS Catal.* 9 (2019) 1564–1577, <https://doi.org/10.1021/acscatal.8b04967>.